frontiers | Frontiers in Energy Research

TYPE Original Research
PUBLISHED 19 March 2024
DOI 10.3389/fenrg.2024.1264157

Power quality improvement using a 31-level multi-level inverter with bio-inspired optimization approach

A. Praveena and K. Sathishkumar*

School of Electrical Engineering, Vellore Institute of Technology, Vellore, India

OPEN ACCESS

EDITED BY
Chee Wei Tan,
University of Technology Malaysia, Malaysia

REVIEWED BY
Minh Quan Duong,
The University of Danang, Vietnam
Norjulia Mohamad Nordin,
University of Technology Malaysia, Malaysia

*CORRESPONDENCE
K. Sathishkumar,
✉ kansathh21@yahoo.co.in

RECEIVED 20 July 2023
ACCEPTED 22 January 2024
PUBLISHED 19 March 2024

CITATION
Praveena A and Sathishkumar K (2024), Power quality improvement using a 31-level multi-level inverter with bio-inspired optimization approach.
Front. Energy Res. 12:1264157.
doi: 10.3389/fenrg.2024.1264157

In recent years, the power quality (PQ) improvements have been explored through various approaches. The employment of electronic devices with renewable energy sources has expanded the harmonics level of voltage and current. Due to harmonics, the PQ of a specific electrical system gets affected. At critical load conditions, the traditional PQ mitigation approaches fail to develop the performance of the system. Therefore, in this work, the Spider Monkey Optimization convolutional neural network (SM-CNN)-based 31-level multilevel inverter (MLI) is used. This method balances the reactive power demands and enhances real power in the grid-tied photovoltaic (PV) system. The maximum power point tracking (MPPT) algorithm depending on radial basis function neural networks (RBFNNs) is used to maximize PV power. For strengthening the voltage level of the PV and to generate higher DC voltage with a minimized switching loss, an integrated boost fly back converter (IBFC) is introduced. The presented technique is implemented in the MATLAB/Simulink platform to figure out the estimation of PQ issues. The suggested MLI lessens the total harmonic distortion (THD) value to 2.45% with an improved power factor.

KEYWORDS

photovoltaic system, multilevel inverter, Spider Monkey Optimization convolutional neural network, radial basis function neural network-MPPT, integrated boost-flyback converter

1 Introduction

In developing technologies, the issue of power electronic devices has shown a greater surge because of the exploitation in real-time applications. Generally, several types of controllers are used to mitigate different power quality (PQ) issues (Babu et al., 2020a). The rapid consolidation of photovoltaics (PV) is mostly based on improvements in PQ and global radiation technology (Ray et al., 2018). Power is converted from DC to AC by use of an inverter and a distribution system. The majority of voltage and current distortion has an impact on the system's performance when it is linked to the grid. As a result of highly volatile devices coupled with an increase in the demand for nonlinear loads, the effectiveness of the system and the power network with regard to PQ is also affected (Badoni et al., 2021).

The unique functions of the PQ impact are consumers and utility equipment. By including renewable energy sources (RES) in the grid, the PQ of the system might be increased. Based on the coupled RES and nonlinear loads, the negative impacts on the system's PQ are improved in this case. A renewable energy source contributes to the amount of reactive power on the line, and the associated harmonics are determined by nonlinear

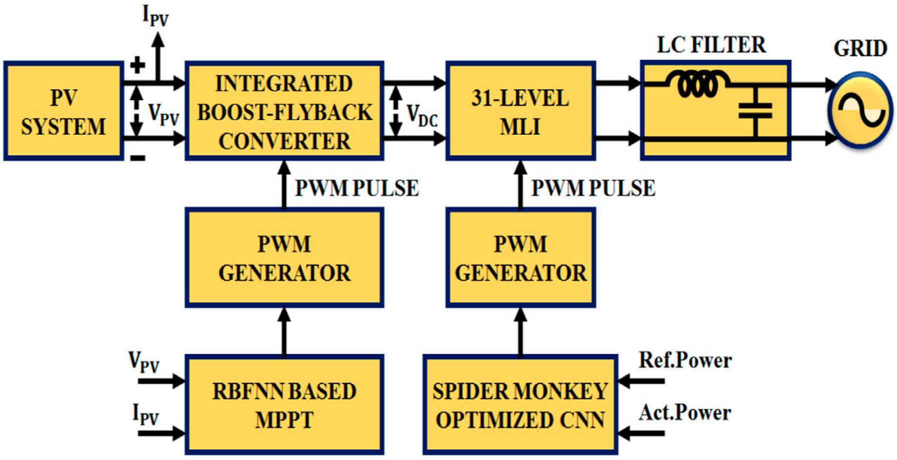

FIGURE 1
Block diagram of suggested Methodology.

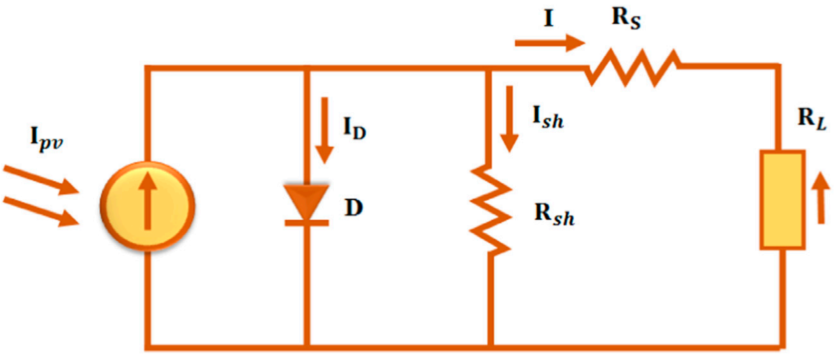

FIGURE 2
Circuit diagram for PV cell.

loads on the grid (Babu et al., 2020b; Golla et al., 2021; Ray et al., 2021). Many other RES-based technologies have been created during the last few years. Some of those sources are becoming more affordable very quickly, and others are widely recognized as low-cost options for grid-related applications (Rajesh et al., 2021).

The output voltage of boost-type converters can be boosted above the input voltage. Nevertheless, because of the internal losses, output voltage, and current stresses suffered by semiconductors, they present a gain restriction (Spiazzi et al., 2010). A high-frequency transformer connected to a flyback converter can be used as a way to receive significantly more voltage. However, because of the energy stored by the converter in its leakage inductance, when blocking voltage is present, the power main switch frequently shows a high reverse voltage (Chen et al., 2015; Shitole et al., 2017).

As a result, using integrated converters is necessary for the purpose of increasing costs and lowering efficiency. Moreover, during commutations, high conversion exposes the diode output to maximum voltage peaks. Furthermore, conventional converters have a limited duty ratio but can increase the output voltage. Furthermore, output voltage and switching stress are also both close. As a result, the given output voltage is considered the duty cycle with a lower value, increasing the converter's efficiency (Hu et al., 2014; Pathy et al., 2016; Shen and Chiu, 2016; Banaei et al., 2019). Therefore, in order to overcome the above issues, the integrated boost-flyback converter (IBFC) is used in this study. The proposed IBFC effectively stabilizes the PV output voltage.

The maximum power extraction method is a main consideration in PV system electricity generation for improving the effectiveness of non-uniform solar irradiance and shading. Overall, numerous control techniques for a grid-coordinated PV system have been proposed (Bouselham et al., 2017). The most commonly used MPPT algorithms in both huge and small-sized PV applications are fuzzy logic control, perturb and observe (P&O), and incremental conductance. It is a difficult task to maintain synchronization, reliability, and overall system behavior in the grid connection (Chandra and Gaur, 2020; Prasad et al., 2021). As a consequence, an efficient control mechanism is required to control PQ issues in a PV system. Thus, the effective RBFNN-MPPT is employed to separate more power from the PV system.

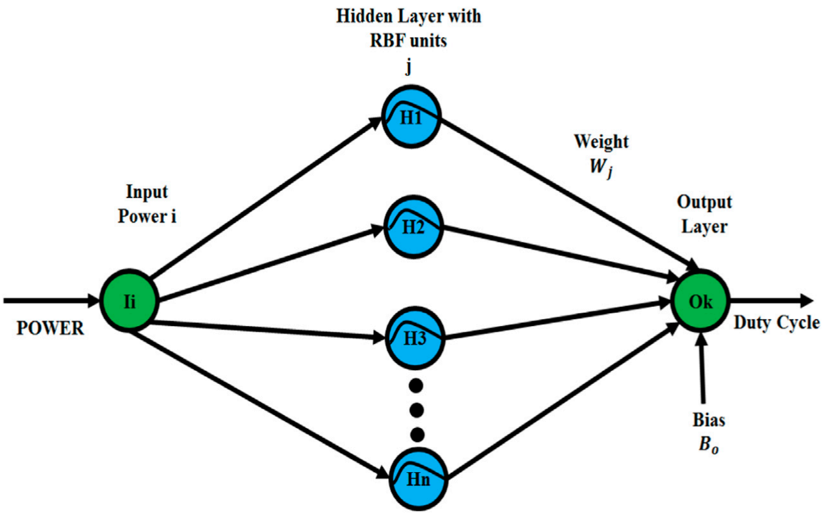

FIGURE 3
RBFNN-based MPPT algorithm.

TABLE 1 Parameter specification.

Parameter	RBFNN
Input data	Power and PV
Target data	Duty cycle, D
Training function	“trainlm”
Hidden layer function	Radial basis “radbas”
MSE performance	0.0121

Domestic and industrial appliances have seen enormous growth over the past few years. Power systems with defects that cause damage produce their elements as an outcome of the overheating process (Kumar et al., 2018; Dhanamjayulu et al., 2019; Khare et al., 2020; Lal and Thankachan, 2021). Additionally, there are certain common problems in these power systems, such as harmonic distortion, voltage sag, transient, and spikes (Arjunagi and Patil, 2021; Parida et al., 2021; Ramasamy and Perumal, 2021; Aarthi et al., 2023). With the help of Spider Monkey optimization CNN, MLI tackles the aforementioned issues and provides a high output voltage. The power quality should be considered to improve the performance based on renewable energy using DC–DC converters, and bridge controllers are used to optimize the energy (Kumar et al., 2012; Shimi et al., 2013).

By the main considerations of various problems, the power quality disturbances are classified by using neural network classifiers, but they mostly conflict massive distortions that occur and fail to improve the performance of power quality (Saravanakumar and Saravana kumar, 2023). However, in some cases, the new learning algorithms are used based on the deep learning system by concerning power quality systems [29]. The CNN model makes deforming scaling learning techniques to classify the distortion, but learning weights are mitigated to adjust the bias weight of power quality elements to improve the performance.

In this paper, the efficient RBFNN-based MPPT is deployed for improving the performance of the grid-tied PV system from PQ issues. The IBFC is used to boost the level of voltage in the PV system. By using the SM-CNN control approach for 31-level MLI, the PQ is successfully improved, and this inverter takes parallel processing PQ difficulties to easily manage the power consumption. Hence, the suggested approach is used to provide the system with enhanced PQ and a reduced THD of 2.45%.

2 Proposed system

The block diagram of the suggested methodology is demonstrated in Figure 1. The grid coordinated with the solar system consists of the PV array, IBFC, 31-level MLI, and LC filter.

For applying the RBFNN-based MPPT algorithm, the highest power is extracted from the PV system, and it is also utilized to strengthen the power conversion efficiency in the solar panel. A single PV panel produces a limited amount of electricity, necessitating the use of a large number of PV panels. The boost-flyback converter is integrated to circumvent this problem, which in turn produces a stable output. The MLI converts the power, in the form of DC into AC, and it is transformed into the grid (i.e., load). The enhanced output from the converter is fed into a 31-level MLI that enhances the PQ and minimizes the lower-order harmonics, with the assistance of SM-CNN.

3 Proposed system modeling

3.1 Modeling of the PV system

The majority of PV arrays include an inverter to transform DC into alternating current, which may be used to power loads like motors, lights, and other appliances. The individual components of a PV array are normally connected in parallel after the modules are

TABLE 2 Modes of operation.

Mode	Conducting switches and diode	Output voltage	Mode	Conducting switches and diode	Output voltage
1	S1, D2, D3, D4, T1, and T2	6 V	1	S1, D2, D3, D4, T3, and T4	-6 V
2	S2, D1, D3, D4, T1, and T2	12 V	2	S2, D1, D3, D4, T3, and T4	−12 V
3	S1, S2, D3, D4, T1, and T2	18 V	3	S1, S2, D3, D4, T3, and T4	−18 V
4	S3, D1, D2, D4, T1, and T2	24 V	4	S3, D1, D2, D4, T3, and T4	−24 V
5	S1, S3, D2, D4, T1, and T2	30 V	5	S1, S3, D2, D4, T3, and T4	−30 V
6	S2, S3, D1, D4, T1, and T2	36 V	6	S2, S3, D1, D4, T3, and T4	−36 V
7	S_1, S_2, S_3, D_4, T_1, and T_2	42 V	7	S1, S2, S3, D4, T3, and T4	−42 V
8	S4, D1, D2, D3, T1, and T2	48 V	8	S4, D1, D2, D3, T3, and T4	−48 V
9	S1, S4, D2, D3, T1, and T2	54 V	9	S1, S4, D2, D3, T3, and T4	−54 V
10	S2, S4, D1, D3, T1, and T2	60 V	10	S2, S4, D1, D3, T3, and T4	−60 V
11	S1, S2, S, D3, T1, and T_2	66 V	11	S1, S2, S4, D3, T3, and T4	−66V
12	S3, S4, D1, D2, T1, and T2	72 V	12	S3, S4, D1, D2, T3, and T4	−72 V
13	S1, S3, S4, D2, T1, and T2	78	13	S1, S3, S4, D2, T3, and T4	−78 V
14	S2, S3, S4, D1, T1, and T2	84 V	14	S2, S3, S4, D1, T3, and T4	−84 V
15	S1, S2, S3, S4, T1, and T2	90 V	15	S1, S2, S3, S4, T3, and T4	−90 V

typically connected in series to achieve the necessary voltages. The corresponding circuit diagram for a PV cell is shown in Figure 2.

A current source in parallel with a diode models an ideal. Nevertheless, no solar cell is perfect, so shunt and series resistances are included in the model, as illustrated in the PV cell schematic above. R_S is the intrinsic series resistance, which has a very small value. R_{Sh} is the equivalent shunt resistance, and it is extremely high.

Applying Kirchhoff's law to the node where I_{pv}, diode R_{Sh}, and R_S reach yields the following equation:

$$I_{pv} = I_D + I_{sh} + I. \tag{1}$$

The PV current equation is given as

$$I = I_{pv} - I_{sh} - I_D, \tag{2}$$

where I_{pv} is the insolation current, I represents the cell current, I_O is reverse saturation current, V denotes the cell voltage, and R_S indicates the series resistance. According to the cell current, the parallel resistance remains to balance the isolation current shown in Eq. 2.

$$I = I_{pv} - I_O.\left[\exp\left(V + I.\frac{R_S}{V_T}\right) - 1\right] - \left[V + I.\frac{R_S}{R_{Sh}}\right]. \tag{3}$$

R_{Sh} represents the parallel resistance, V_T represents the thermal voltage (KT/q), K represents the Boltzmann constant, T represents the temperature in Kelvin, and q represents the charge of an electron. The forthcoming section provides the detailed description about the RBFNN-MPPT algorithm, which separates the maximum power from the PV panel.

3.2 Model of the radial basis function neural network-based MPPT technique

Figure 3 demonstrates the architecture for the RBFNN-based MPPT algorithm. The proposed RBFNN-MPPT is a three-layer network with a hidden layer, input layer, and output layer.

It is an algorithm for supervised learning, which is employed to train multi-layer activation functions. When a specific set of inputs (power) is applied to the RBFNN-based MPPT technique, it produces the expected output (duty cycle) by fine-tuning its weights. Using PV module power and converter duty cycle as input variables and irradiance variations as the output variables, the RBFNN is trained. The parameters used in the RBFNN training are listed in Table 1.

Steps for the RBFNN

Step 1: Generation of random weights to small random values to make sure t hat the network is unsaturated by large weight value.

Step 2: A training pair from the training set is selected

Step 3: The input vector to the network input is applied

Step 4: The network output is calculated

Step 5: Error is computed as the subtraction between the network output and desired output.

Step 6: Network weights are adjusted in order to minimize the error.

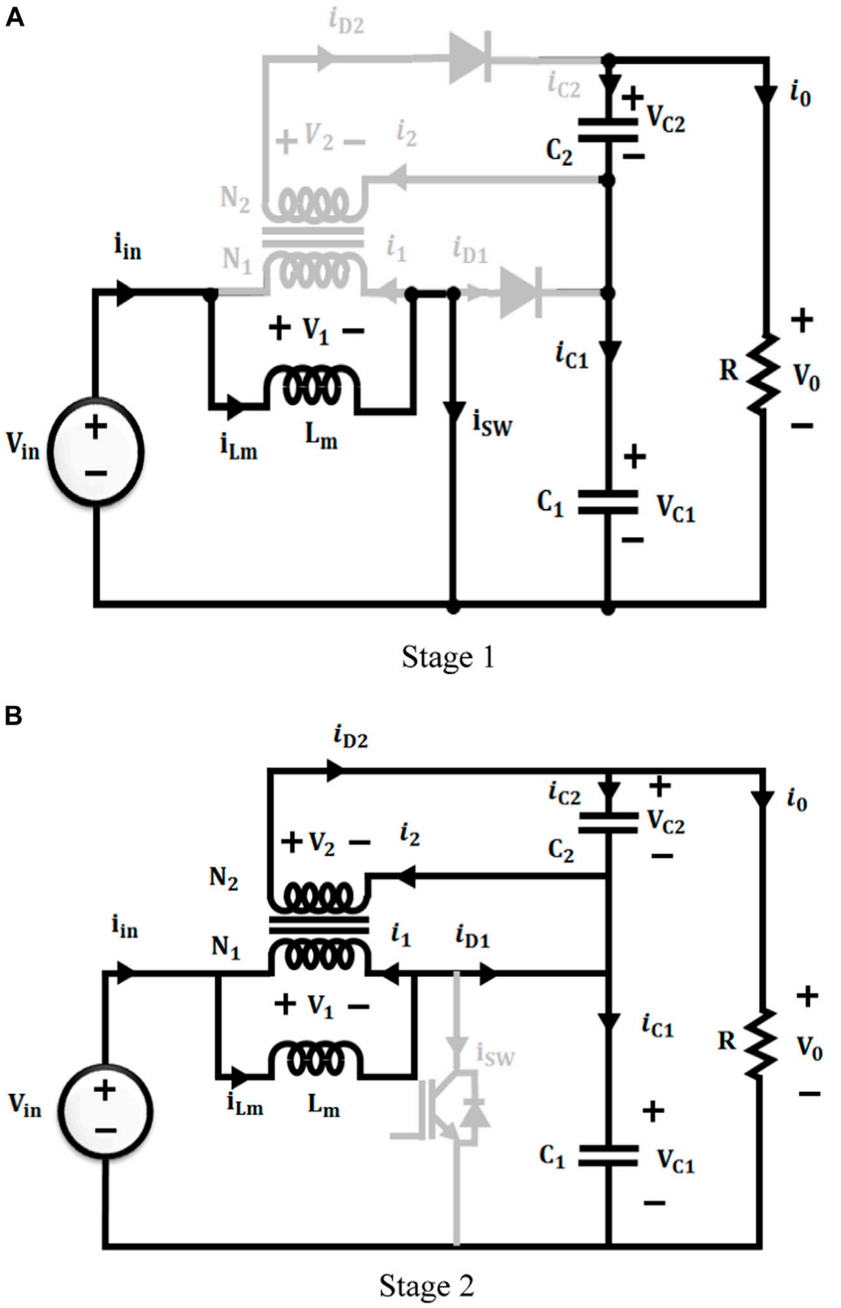

FIGURE 4
IBFC.

Step 7: Return to steps 2-6 for the individual input-output pair of the training set until the error for the whole system is tolerabley.

The RBFNN's hidden layer has unique activation functions including Gaussian, multi-quadratics, and inverse multiquadratics. When compared to the traditional BPNN, the RBFNN is a better activation function with reduced distance from function establishments.

The hidden layer is composed of a Gaussian activation function that is focused in feature space on a vector. There are no extra weights from the input layer to the hidden layer. The input layer is delivered directly to the $j-th$ Gaussian hidden unit. The RBF's $k-th$ unit output is indicated as follows:

$$O_k = B_O + \sum_{j=1}^{h} W_{jk}{}^{*} H_j, \tag{4}$$

where H_j represents the radial basis output of the $j-th$ hidden unit and is given by $H_j = f(||I - c_j||)$ Here, $c \in R$ refers to the center of the RBF with radius r.

$$f(x) = e^{\left(\frac{||I_i - c_j||^2}{r^2}\right)}. \tag{5}$$

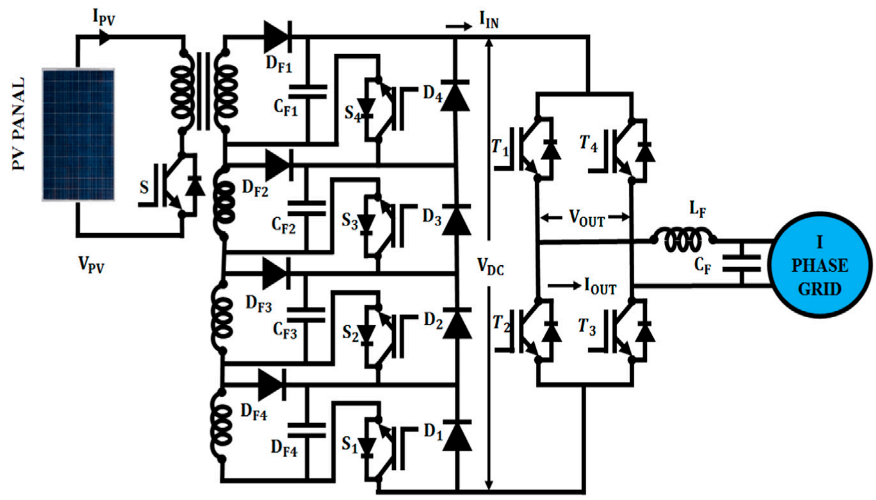

FIGURE 5
Proposed MLI.

3.2.1 Performance testing

The mean squared error (MSE) impacts the performance of the NN. By modifying the output-layer weight W_{jk}, the MSE is minimized depending on the inputs I and T target vector is presented as follows:

$$E = 1\big/m\sum_{k=1}^{m}(T_k - O_k)^2, \tag{6}$$

where $t(k)\, and\, o(k)$ represent a target and network output kth sample, respectively, and m represents the total training patterns.

Table 2 represents the parameter specification for RBFNN MPPT techniques. The highest power attained from the PV system is enhanced with the advisable IBFC, which is employed to convert the PV output voltage into an AC form with higher efficiency and low switching losses.

3.2.1.1 Modeling OF IBFC

Figure 1 shows that the IBFC shares the power IGBT switch and the inductor to integrate a boost and flyback converter.

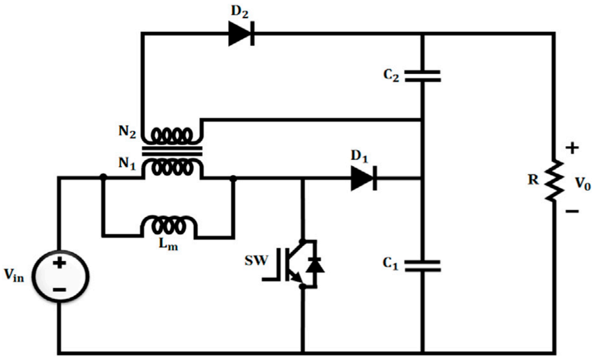

The inductor employed in this instance is a type of a linked inductor, which has two windings wound around a single magnetic core. L_m represents the connected inductor's magnetizing inductance. There are, respectively, N_1 and N_2 turns in the primary and secondary windings. C_T and C_2 are connected in series to produce the IBFC output. The magnetizing current i_{Lm} runs continuously and stays above 0 throughout a switching cycle in the continuous conduction mode (CCM). The operation of the IBFC can be divided into stages.

3.2.1.2 Stage 1

While SW is activated, D_1 and D_2 are reverse-biased. V_{in} is used to power the linked inductor's primary winding, i_{Lm} increases linearly, and L_m stores the energy. The linked inductor's primary and secondary currents, i_1 and i_2, respectively, are both 0 since D2 is reverse-biased. The load resistance, R, discharges C_1 and C_2 throughout this time, supplying the load current.

3.2.1.3 Stage 2

Figure 4 when SW is disabled, i_{Lm} continues to flow in the same direction by compelling D_1 and D_2 to conduct. During this time, the energy held in L_m is released to charge C_1 and C_2 as i_{Lm} linearly diminishes.

With the use of this approximation, the current waveform analysis and device ratings, such as $SW, D_1, and\, D_2$, are made easier.

The following equation represents the voltage gain of the IBFC as follows:

$$\frac{V_O}{V_{in}} = \frac{1+nD}{1-D}, \tag{7}$$

$$V_O = V_{in}\left(\frac{1+nD}{1-D}\right), \tag{8}$$

where D is the duty cycle of the SW and $n = N_1/N_2$ is the linked inductor's turn ratio. By modifying the duty ratio D of the switch, the average output voltage of the IBFC is changed.

3.2.2 Modeling of the 31-level MLI

Asymmetric semiconductor devices using the same voltage sources and quantity can also produce high output levels when compared to their symmetric counterparts. The MLI structure,

TABLE 3 Design parameter.

Parameter	Specification
Solar PV system	
Series-connected solar PV cells	36
Open circuit voltage	$12V$
Short circuit current	$8.33A$
Peak power	10 KW and 10 panels
Integrated boost-flyback	
$L_1, L_2, L_3, \& L_4$	$2^*(350uH - 6A) + 2^*(350uH - 2A)$
• $C_1, C_2, C_3, \& C_4$	• $47uF$
• $C_{o1} \& C_{o2}$	• $180u$
• C_{in}	• $470\,uF$

constructed with an H-bridge inverter circuit defined as the polarity generation circuit and an asymmetric fundamental circuit called as the level generator unit, is illustrated in Figure 5. Switches in the polarity generation circuit, especially contrasted to other switches in the level generation unit, are under more stress.

The circuit contains an equal number of driver circuits and IGBTs as all of its semiconductor switching components are positioned in the same direction. The switching losses in a multilevel inverter circuit depend on three different parameters: switching frequency, current, and blocking voltage. The locations of each and every switch in the level generation unit are displayed in Table 3. A total of 15 levels are generated using the level generation units $S_1, S_2, S_3, and\, S_4$ and the polarity generation units T_1 and T_2. Switching OFF $S_1, S_2, S_3, and\, S_4$ results in the 0 level. Half cycles, both positive and negative, are also symmetrical.

As an illustration, the switches $S_1 and\, S_2$ are turned ON, and state 3 of the diodes D_3 and D_4 are forward-biased. In the positive half-cycle, $V_O = V_1 + V_2$ is obtained. This method is repeated for each additional state to achieve the output voltage values.

In a positive cycle, the H-bridge inverter's switches T_1 and T_2 are turned ON, while T_3 and T_4 are turned OFF. T_1 and T_2 are turned OFF, while T_3 and T_4 are turned ON during the negative cycle. The following Table 3 demonstrates the 31-MLI's method of operation.

The circuit is going to operate in mode 1, and the amplitude of 6 V will now be linked to the grid through the inverter switches T_1 and T_2 during the positive half-cycle when the switches S_1, D_2, D_3, and D_4 of the multiplier are switched ON. The circuit will transition to mode 2, and the output voltage of 12 V will be accessible at the inverter output when switches S_2, D_1, D_3, and D_4 are turned ON. Similarly, by turning on the switches S_1, S_2, D_3, and D_4 of the multiplier cell in mode 3, the output of 18 V will be made available. The switches are activated in this order until all 15 modes have been used. For negative cycles, the same switching sequence is repeated.

3.2.3 SM optimized CNN

3.2.3.1 CNN

The CNN classifier efficiently differentiates the harmonics with the help of the features including standard deviation, mean, entropy, energy, and log-entropy. The feedforward network of the CNN basically has three layers, such as maximum, pooling, and convolutional layers, which are fully connected. The CNN architecture is illustrated in Figure 5.

The backpropagation method is used to train the parameters. The factor of two values is down-sampled by pooling layers, which is regarded as the down-sampling layer, and the maximum value of the convolutional layer is sent to the next layer. The number of training samples and times is reduced by this proposed strategy. These samples are carried on to the following layer, which is fully connected and has multiple hidden layers. Weights are used to connect the hidden and output layers, the final output classifier layer, and the pooled samples to a fully connected network. The forward and backpropagation are the two steps of the training process, where forward propagation provides the actual input data and backpropagation updates the training parameters.

Using all of the input coefficients has a negative influence on the classification accuracy every time. As a result, the chosen coefficients mean (M), standard deviation (SD), energy (E), entropy (ET), and log-energy entropy (LE) are eliminated to reduce complexity and improve classification accuracy. The primary component expressions are described as follows:

Mean

$$M_{ki} = -\frac{1}{N}\sum_{j=1}^{N} X_{ij}. \tag{9}$$

Energy

$$K_{ki} = \sum_{j=1}^{N}\left(\left|X_{ij}\right|^2\right). \tag{10}$$

Standard deviation

$$\sigma_{ki} = \left(\frac{1}{N}\sum_{j=1}^{N}\left(X_{ij} - \mu_i\right)^2\right)^{\frac{1}{2}}. \tag{11}$$

Entropy

$$ET_{ki} = -\sum_{j=1}^{N} X_{ij}{}^2 \log\left(X_{ij}{}^2\right). \tag{12}$$

Log-energy entropy

TABLE 4 Efficiency analysis.

Analysis	Methods			
	P & O controller (Kumar et al., 2012)	MPPT scheme (Shimi et al., 2013)	CS-HHO-based MPPT scheme	RBFNN-MPPT
Total input power (W)	162.56	162.51	162.59	162.63
Output power (W)	156.73	155.71	157.12	159.65
Efficiency (%)	96.40%	95.21%	96.81%	97.2%

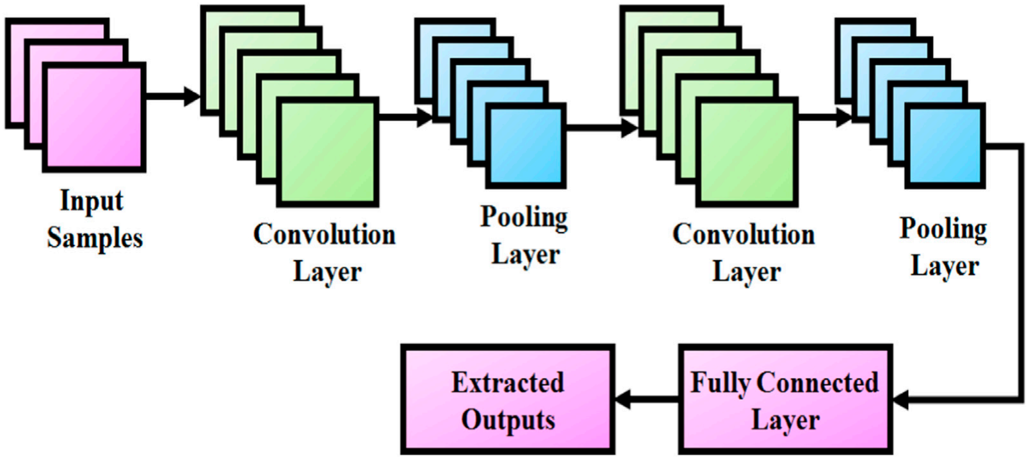

FIGURE 6
CNN Architecture.

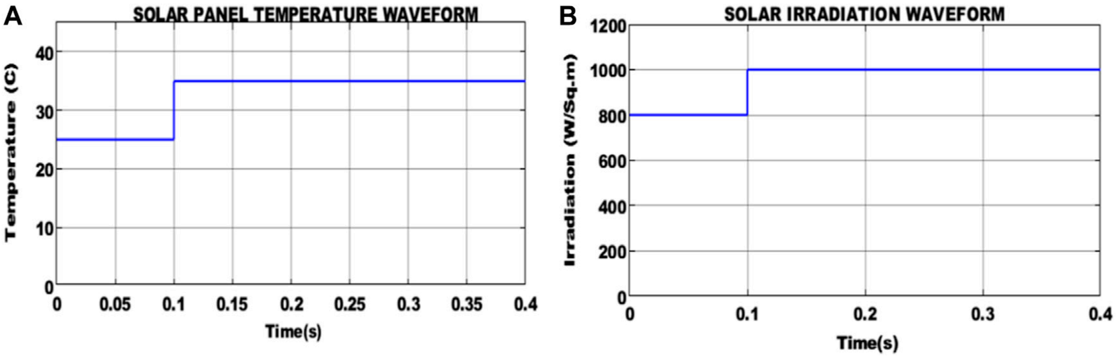

FIGURE 7
(A) Temperature and **(B)** irradiation waveforms for the solar panel.

$$LE_{ki} = -\sum_{j=1}^{N} \log\left(X_{ij}^{2}\right). \tag{13}$$

In this paper, the reference and real signals are transmitted to the CNN classifier to reduce the harmonics and provide reference power to the PWM generator that produces gating pulses for the 31-level MLI. Furthermore, the CNN has to be optimized to enhance the control performance of the MLI.

4 SMO algorithm

The SMO methodology is a metaheuristic method that uses fission and fusion swarm intelligence for foraging. This algorithm is inspired from the behavior of spider monkey. The following are six iterative collaborative phases, and the SMO method relies on trial and error.

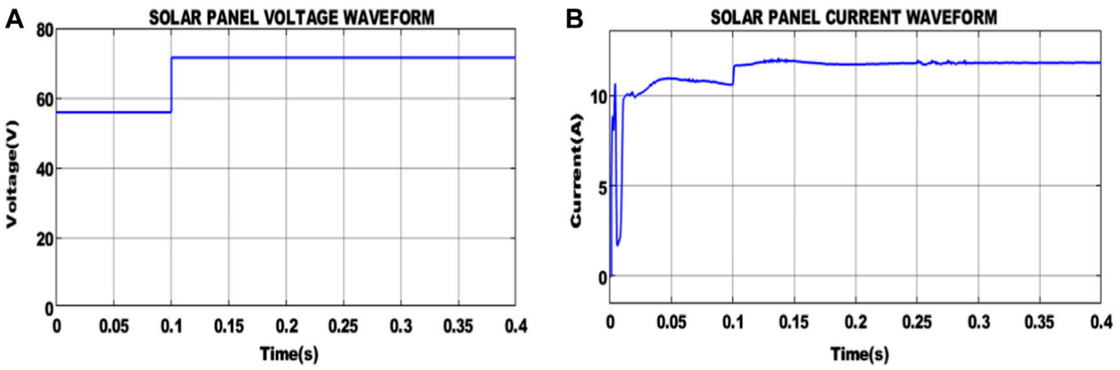

FIGURE 8
(A) Voltage and **(B)** current waveforms for the solar panel.

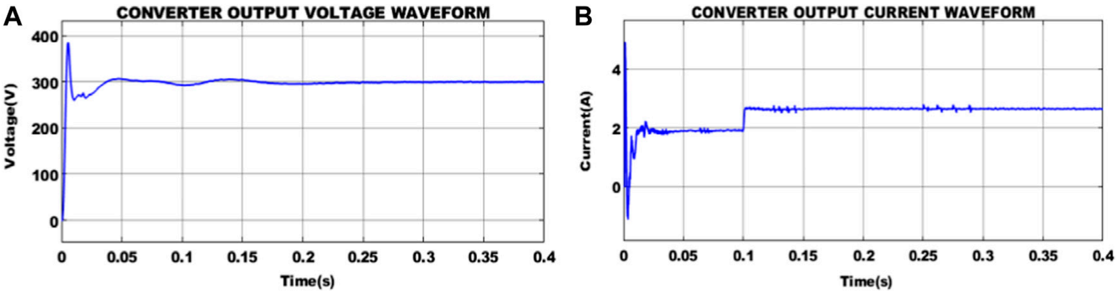

FIGURE 9
(A) Voltage and **(B)** current output of IBFC.

4.1 Initializing

The SMO initializes each SM_p using Eq. 14

$$SM_{pq} = SM_{minq} + UR(0,1) \times \left(SM_{maxq} - SM_{minq}\right), \tag{14}$$

where SM_{pq} is the qth dimension's $pth\,SM$, for random, the upper and lower bounds of SM_p of SM_{minq} and SM_{maxq} in the qth direction, respectively. The number of UR is between [0, 1], with a uniform distribution.

4.2 Local leader phase)

SM includes the historical occurrences of local group members and leaders to shift the place. If the new position value is higher than the past one, the SM location of the lth local group is updated.

$$SM_{newpq} = SM_{pq} + UR(0,1) \times \left(LL_{lq} - SM_{pq}\right) + UR(-1,1) \times \left(SM_{rq} - SM_{pq}\right). \tag{15}$$

The local group lth of the qth dimension is selected for lth. SM is random and is represented as SM_{rq}, such that r, p. LL_{lq} is the qth dimension of the lth local group leader location.

4.3 Global leader phase

Following LLP, the GLP is initiated to update the location. Equation 16 provides the location update as follows:

$$SM_{newpq} = SM_{pq} + UR(0,1) \times \left(GL_{lq} - SM_{pq}\right) + UR(-1,1) \times \left(SM_{rq} - SM_{pq}\right), \tag{16}$$

where GL_{lq} represents the qth dimension of the GLP and q is a randomly chosen index between $1\ and\ M$.

4.4 Global leader learning phase

By utilizing the strategy of greedy selection, GLL is updated. The new SM depends on the country with the fittest people in the world. If updates are discovered, the global limit count (GLC) is increased and the value of the global leader is applied to the optimum setting.

4.5 Local leader learning phase

The SM location is updated with the position of the local leader for optimal fitness in a specific group. The ideal location is given to the local leader. If no updates are found, an increment of 1 is applied to the limit count.

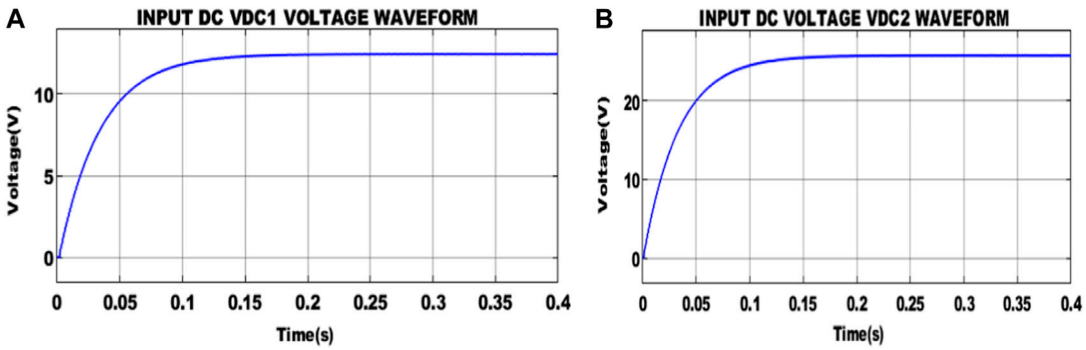

FIGURE 10
Input **(A)** VDC1 & **(B)** VDC2 waveform.

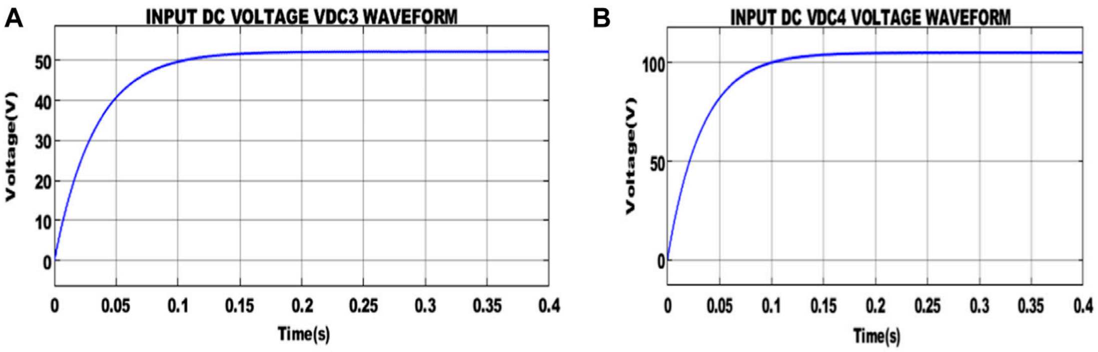

FIGURE 11
Input **(A)** VDC3 & **(B)** VDC4 waveforms.

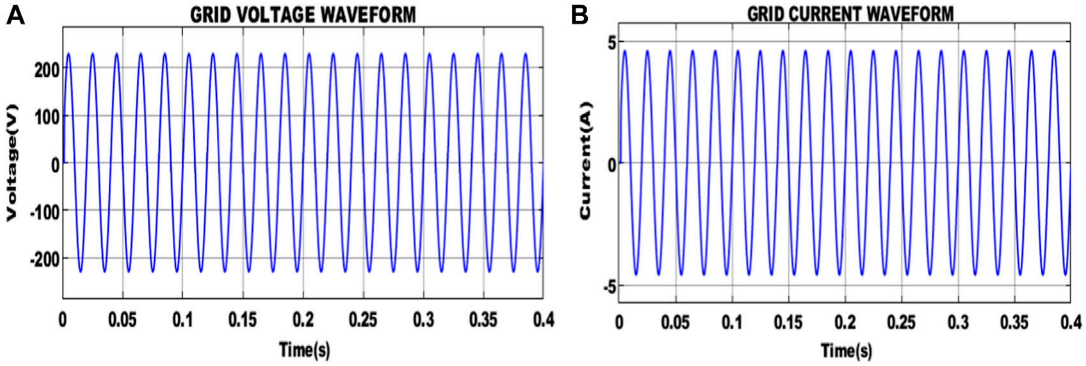

FIGURE 12
Grids: **(A)** voltage and **(B)** current.

4.6 Local leader decision phase

When a local leader does not update its location or outdated from global and local leaders depending on P_r using Eq. 17, the candidates of the local group change the position at a random step 1.

$$SM_{newpq} = SM_{pq} + UR(0,1) \times \left(GL_{lq} - SM_{pq}\right) + UR(0,1) \times \left(SM_{rq} - LL_{pq}\right). \tag{17}$$

4.7 Global leader decision phase

In accordance with GLD, the population is split into smaller groups. For the global leader limit, the location value is unchanged. The dividing process starts after there are as many groups (MG) as possible. For the newly created group, a local leader is selected during each cycle. It does not modify its position until the allowable maximum is reached, at which point it tries to merge all of the permitted groups into a single

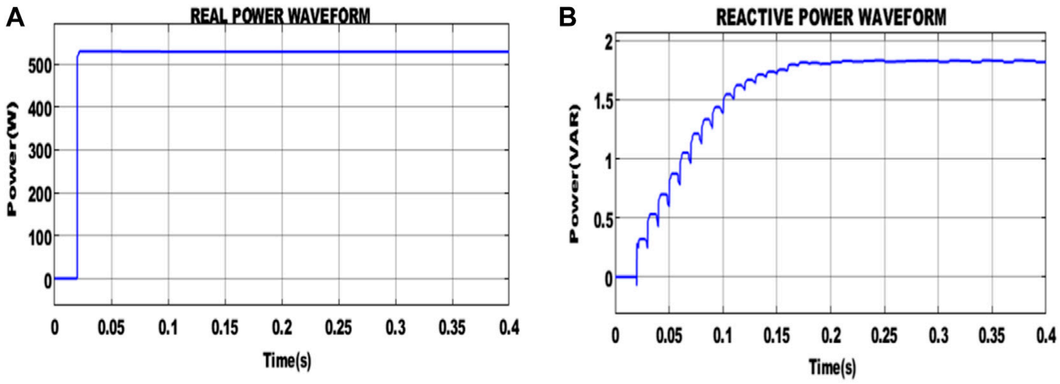

FIGURE 13
Real and reactive power waveforms.

TABLE 5 Statistical analysis.

Methods	ANN	CS-RNN	SM-CNN
Mean	1.5625	0.5136	0.4342
Median	1.8500	0.2175	0.1702
Standard deviation	0.9254	0.4102	0.3152

group. The maximum number of permitted groups is established.

4.8 Gaussian mutation

In complex iterative optimization situations, the SMO approach is imprisoned in the local best value. The algorithm solution value does not vary throughout the iteration. This approach leaves the location of the local optimum, adds GM and random perturbation, and then extends to execute the algorithm in order to enhance the algorithm probability and algorithm deficiency. Equation 18 provides the formula for the Gaussian mutation.

$$x^{i,iter+1} = \begin{cases} x^{i,iter} + rand & if\ r \geq 0.2 \\ x^{i,iter} \times Gaussian(\mu, \sigma) & otherwise \end{cases}. \tag{18}$$

where *rand* represents a random number between [0, 1], and r_j represents the probability of random perturbation or Gaussian mutation selection. Equation 19 provides the Gaussian variation distribution.

$$Gaussian(\mu, \sigma) = \left(\frac{1}{\sqrt{2\pi\sigma}}\right) \exp\left(-\frac{(x-\mu)^2}{2\sigma^2}\right), \tag{19}$$

where σ^2 stands for the variance and μ stands for the mean value. With the support of SMO, the CNN parameters are optimally tuned for the generation of improved THD and unity power factor.

5 Results and Discussion

This proposed work aimed at the improvement of an efficient spider monkey optimization CNN, which is deployed to improve the PQ in the grid-tied PV system. In addition, the RBFFN-based MPPT algorithm is employed to track the highest power from the

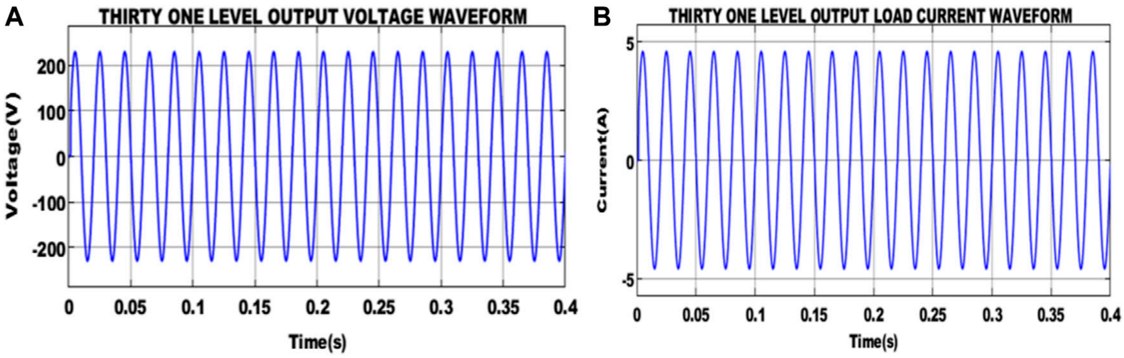

FIGURE 14
31-level output **(A)** voltage and **(B)** load current waveforms.

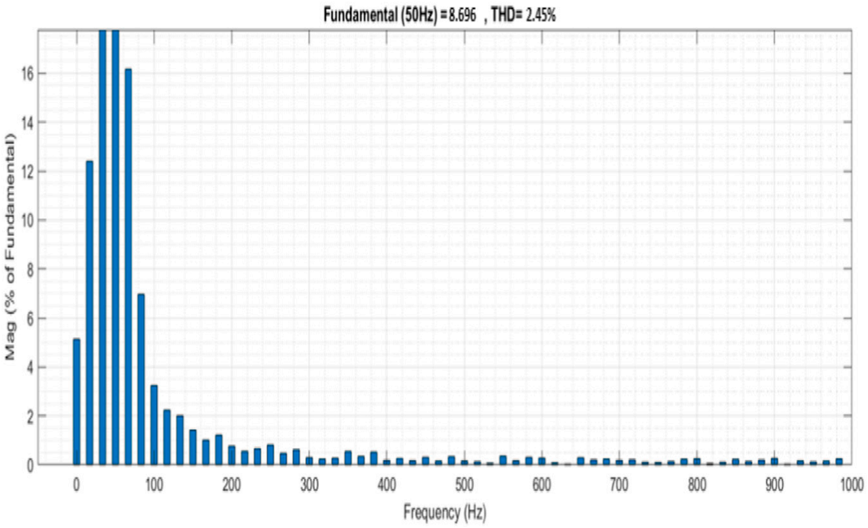

FIGURE 15
THD waveform.

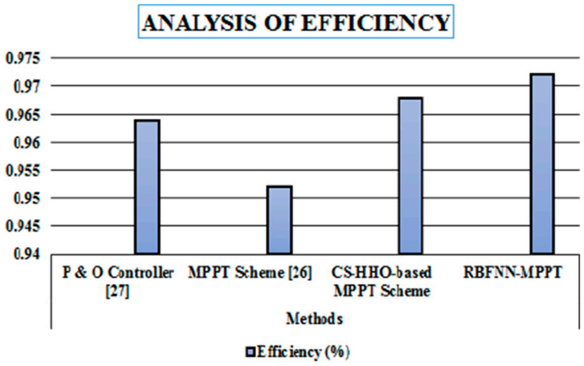

FIGURE 16
Efficiency analysis.

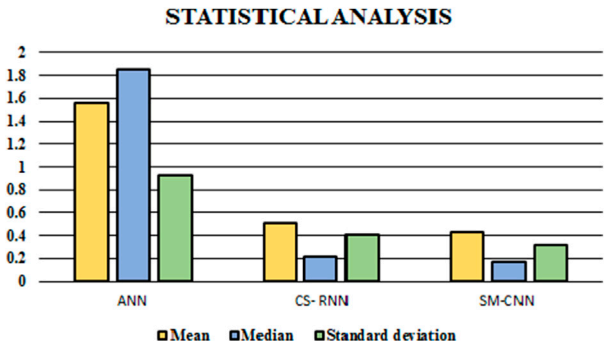

FIGURE 17
Statistical analysis.

PV system. The suggested control technique is verified using the MATLAB platform. Table 4 represents the parameter specification for the proposed system.

A temperature variation of 0.1 s is introduced, as shown in Figure 6A, to calculate the efficiency of the suggested technique in handling the intermittent nature of the PV system. At this same moment, the temperature suddenly increases from 25°C to 35°C. Similar to how temperature varies, Figure 6B shows that solar irradiation varies from 800 W/sq.m to 1000 W/sq.m.

Figure 7 displays the solar panel voltage and currents as a variation in temperature. Due to operating conditions, the voltage is suddenly increased from 58 V to 72 V; similarly, the current increases to 15 A, afterward, the current remains constant at 0.1 s.

The waveform that represents the voltage output of the IBFC is presented in Figure 8A. From that waveform, the voltage of 300 V is achieved at 0.2 s, and Figure 8B shows output current variations until 0.1 s, after which the stable value of 2.5 A is maintained.

Figure 9 illustrates that the input DC voltage is obtained from the integrated boost-flyback converter. VDC1 and VDC2 with the constant value of 15 V and 16 V, respectively, are maintained. Likewise, Figure 10 shows the DC voltage VDC3 and VDC4 with the stable value of 52 V and 102 V are maintained.

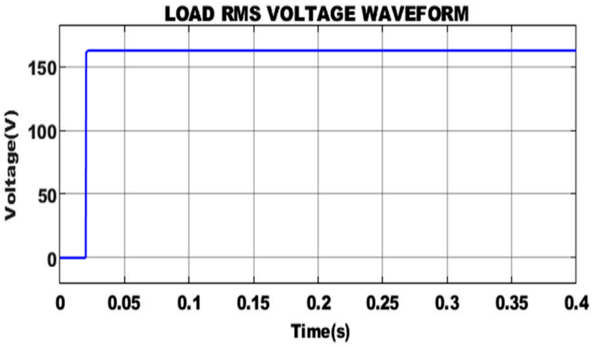

Figure 10 shows the load RMS voltage waveform. From that graph, the load RMS voltage 175 V is accomplished at 0.02s.

From the waveform representation shown in Figure 11, it is noted that a constant voltage of 230 V is supplied to the grid. Similarly, the grid current value of 4 A is maintained.

Figure 12 depicts the waveforms that represent the reactive and real power of grid 1. At 0.03 s, the magnitude of real power stabilizes at 520 W, and the minimized reactive power is achieved.

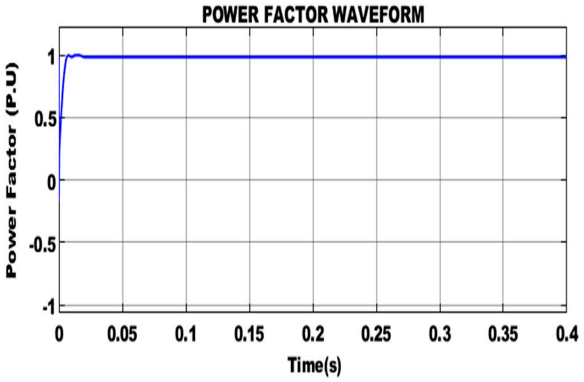

The waveform of the power factor is shown in Figure 13. Thus, a power factor of 1 is attained, denoting that the suggested system operates with efficiency and dependability.

Figure 14 shows the output current and voltage waveform of the 31-level MLI. Here, the voltage of 220 V is maintained as shown in Figure 14A, and the load current of 4.5 A is achieved, as shown in Figure 14B.

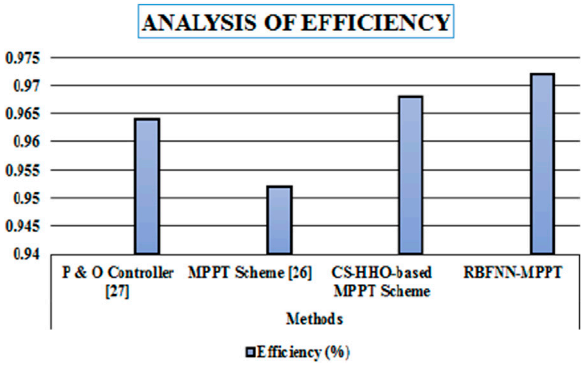

Figure 15 indicates the proposed IBFC converter's THD value as 2.45%, which has very low harmonics when compared to that of other approaches.

Table 5 compares several power tracking methods, and Figure 16 shows the corresponding graphs with similar comparisons. As the RBFNN-based MPPT efficiency is 98.80%, Table 5 and Figure 17 demonstrate the various measures, including mean, median, and standard deviation. The considered factors strongly show that the suggested method outperforms the existing methods in terms of the considered factors.

6 Conclusion

We conclude that the proposed system improves high performance to achieve efficiency. The MLIs have been heavily used to improve the PQ of PV systems. The requirement for a large number of components, increased standing voltage, and high harmonic content in the output cause a significant impact on the efficiency of a standard MLI. In this work, a control approach called Spider Monkey Optimization CNN is used with an appropriate level of inverter (31 level) to lessen PQ problems to solve the mitigations. The integrated boost-flyback converter is employed, in order to stabilize the output voltage of the PV panel to achieve the performance. Intended for separating the highest power from the solar PV system, the RBFNN-based MPPT technique is used, and this achieves an efficiency of 97.2%, which is the highest efficiency compared to that of other control methods. The proposed MLI is produced with an enhanced power factor and a lower THD value of 2.45%, and the influence of harmonics is also negligible.

Data availability statement

The original contributions presented in the study are included in the article/Supplementary Material; further inquiries can be directed to the corresponding author.

Author contributions

PA: writing–original draft. SK: writing–original draft.

Funding

The author(s) declare that no financial support was received for the research, authorship, and/or publication of this article.

Conflict of interest

The authors declare that the research was conducted in the absence of any commercial or financial relationships that could be construed as a potential conflict of interest.

Publisher's note

References

Aarthi, C., Ramya, V. J., Falkowski-Gilski, P., and Divakarachari, P. B. (2023). Balanced spider monkey optimization with Bi-lstm for sustainable air quality prediction. *Sustainability* 15 (2), 1637. doi:10.3390/su15021637

Arjunagi, S., and Patil, N. B. (2021). Optimized convolutional neural network for identification of maize leaf diseases with adaptive ageist spider monkey optimization model. *Int. J. Inf. Technol.* 15, 877–891. doi:10.1007/s41870-021-00657-3

Babu, N., et al. (2020a). An improved adaptive control strategy in grid-tied PV system with active power filter for power quality enhancement. *IEEE Syst. J.* 15 (2), 2859–2870.

Babu, N., Guerrero, J. M., Siano, P., Peesapati, R., and Panda, G. (2020b). A novel modified control scheme in grid-tied photovoltaic system for power quality enhancement. *IEEE Trans. Industrial Electron.* 68 (11), 11100–11110. doi:10.1109/tie.2020.3031529

Badoni, M., et al. (2021). Grid tied solar PV system with power quality enhancement using adaptive generalized maximum Versoria criterion. *CSEE J. Power Energy Syst.*

Banaei, M. R., Zoleikhaei, A., and Sani, S. G. (2019). Design and implementation of an interleaved switched-capacitor dc-dc converter for energy storage systems. *J. Power Technol.* 99 (1), 1.

Bouselham, L., Hajji, M., Hajji, B., and Bouali, H. (2017). A new MPPT-based ANN for photovoltaic system under partial shading conditions. *Energy Procedia* 111, 924–933. doi:10.1016/j.egypro.2017.03.255

Chandra, S., and Gaur, P. (2020). Radial basis function neural network technique for efficient maximum power point tracking in solar photo-voltaic system. *Procedia Comput. Sci.* 167, 2354–2363. doi:10.1016/j.procs.2020.03.288

Chen, Z., Zhou, Q., and Xu, J. (2015). Coupled-inductor boost integrated flyback converter with high-voltage gain and ripple-free input current. *IET power Electron.* 8 (2), 213–220. doi:10.1049/iet-pel.2014.0066

Dhanamjayulu, C., Arunkumar, G., Jaganatha Pandian, B., Ravi Kumar, C. V., Praveen Kumar, M., Rini Ann Jerin, A., et al. (2019). Real-time implementation of a 31-level asymmetrical cascaded multilevel inverter for dynamic loads. *IEEE Access* 7, 51254–51266. doi:10.1109/access.2019.2909831

Golla, M., Chandrasekaran, K., and Simon, S. P. (2021). PV integrated universal active power filter for power quality enhancement and effective power management. *Energy Sustain. Dev.* 61, 104–117. doi:10.1016/j.esd.2021.01.005

Hu, Y., Xiao, W., Cao, W., Ji, B., and Morrow, D. J. (2014). Three-port DC–DC converter for stand-alone photovoltaic systems. *IEEE Trans. Power Electron.* 30 (6), 3068–3076. doi:10.1109/tpel.2014.2331343

Khare, N., Devan, P., Chowdhary, C., Bhattacharya, S., Singh, G., Singh, S., et al. (2020). Smo-dnn: spider monkey optimization and deep neural network hybrid classifier model for intrusion detection. *Electronics* 9 (4), 692. doi:10.3390/electronics9040692

Kumar, A. N., et al. (2018). "A 31-level MLI topology with various level-shift PWM techniques and its comparative analysis," in 2018 3rd International Conference on Communication and Electronics Systems (ICCES), Coimbatore, India, 15-16 October 2018 (IEEE).

Kumar, J. H., Sai Babu, Ch, and Kamalakar Babu, A. (2012). *Design and analysis of P&O and IP&O MPPT techniques for photovoltaic system.* Berlin, Germany: Springer.

Lal, J. D., and Thankachan, D. (2021). *Statistical evaluation of energy harvesting system models in wireless networks: an empirical perspective.*

Parida, N., Mishra, D., Das, K., Rout, N. K., and Panda, G. (2021). On deep ensemble CNN–SAE based novel agro-market price forecasting. *Evol. Intell.* 14, 851–862. doi:10.1007/s12065-020-00466-w

Pathy, S., et al. (2016). "A modified module integrated—interleaved boost converter for standalone photovoltaic (PV) application," in 2016 IEEE International Conference on Renewable Energy Research and Applications (ICRERA), Birmingham, United States, 20-23 November 2016 (IEEE).

Prasad, D., Dhanamjayulu, C., Padmanaban, S., Holm-Nielsen, J. B., Blaabjerg, F., and Khasim, S. R. (2021). Design and implementation of 31-level asymmetrical inverter with reduced components. *IEEE Access* 9, 22788–22803. doi:10.1109/access.2021.3055368

Rajesh, P., Shajin, F. H., and Umasankar, L. (2021). A novel control scheme for PV/WT/FC/battery to power quality enhancement in micro grid system: a hybrid technique. *Energy Sources, Part A Recovery, Util. Environ. Eff.*, 1–17. doi:10.1080/15567036.2021.1943068

Ramasamy, S., and Perumal, M. (2021). CNN-based deep learning technique for improved H7 TLI with grid-connected photovoltaic systems. *Int. J. Energy Res.* 45 (14), 19851–19868. doi:10.1002/er.7030

Ray, P., Ray, P. K., and Kumar Dash, S. (2021). Power quality enhancement and power flow analysis of a PV integrated UPQC system in a distribution network. *IEEE Trans. Industry Appl.* 58 (1), 201–211. doi:10.1109/tia.2021.3131404

Ray, P. K., Soumya, R. D., and Mohanty., A. (2018). Fuzzy-controller-designed-PV-based custom power device for power quality enhancement. *IEEE Trans. Energy Convers.* 34 (1), 405–414. doi:10.1109/tec.2018.2880593

Saravanakumar, T., and Saravana kumar, R. (2023). Fuzzy based interleaved step-up converter for electric vehicle. *Intelligent Automation Soft Comput.* 35, 1103–1118. doi:10.32604/iasc.2023.025511

Shen, C.-L., and Chiu, P.-C. (2016). Buck-boost-flyback integrated converter with single switch to achieve high voltage gain for PV or fuel-cell applications. *IET Power Electron.* 9 (6), 1228–1237. doi:10.1049/iet-pel.2015.0482

Shimi, S. L., Thakur, T., Kumar, J., and Chatterji, S. (2013). "MPPT based solar powered cascade multilevel inverter," in Emerging Research Areas and 2013 International Conference on Microelectronics, Communications and Renewable Energy (AICERA/ICMiCR), Kanjirapally, India, 4-6 June 2013.

Shitole, A. B., Sathyan, S., Suryawanshi, H. M., Talapur, G. G., and Chaturvedi, P. (2017). Soft-switched high voltage gain boost-integrated flyback converter interfaced single-phase grid-tied inverter for SPV integration. *IEEE Trans. industry Appl.* 54 (1), 482–493. doi:10.1109/tia.2017.2752679

Spiazzi, G., et al. (2010). "Improved integrated boost-flyback high step-up converter," in 2010 IEEE International Conference on Industrial Technology, Vina del Mar, Chile, 14-17 March 2010 (IEEE).